ChemCatChem

Research Article
doi.org/10.1002/cctc.202501022

Chemistry Europe
European Chemical Societies Publishing

www.chemcatchem.org

Effect of pH on the Electrochemical Reduction of Nitrate on Metallic Copper

Gabriel F. Costa,[a] Manuel E. G. Winkler,[a, b] Maria R. Pinto,[a] Fabio H. B. Lima,[c]
and Raphael Nagao*[a, b]

The electrochemical reduction of nitrate (NO_3^-) presents a promising route for wastewater treatment and nitrogen cycle restoration. In this work, we investigate the influence of pH on the electrochemical nitrate reduction reaction (NO_3RR) using metallic copper as a model catalyst. We systematically examine pH effects within the range of 4.4 to 9.3 through electrochemical experiments, such as *on line* differential electrochemical mass spectrometry (DEMS) and in situ Fourier transform infrared (FTIR) spectroscopy. Our findings reveal that the NO_3RR mechanism is highly dependent on the electrolyte pH, dictating the rate-determining step and the formation of reaction intermediates. Under mildly acidic conditions (pH 4.4), NO formation is favored, while at mildly alkaline pH (9.3), byproducts such as N_2O and N_2H_4 emerge due to lower proton concentration that hinders oxygenated intermediate hydrogenation. In situ FTIR spectroscopy reveals local pH alkalinization during NO_3RR, shifting phosphate equilibria and influencing reaction selectivity. These insights emphasize the critical role of electrolyte pH in tuning product distribution and reaction pathways. Our work highlights the importance of electrolyte engineering for optimizing electrochemical nitrate reduction, contributing to sustainable nitrogen management strategies.

1. Introduction

The fixation of inert atmospheric nitrogen (N_2) at industrial scales to supply the intensive use of fertilizers has caused a global imbalance in the nitrogen cycle.[1,2] It fixes around 10^8 tons of nitrogen into reactive species per year,[3] which accumulate in aquatic systems over time. In 2017, the National Academy of Engineering recognized the management of the nitrogen cycle as a grand challenge for engineers.[4] Therefore, it is urgent to develop improved technologies for wastewater treatment to minimize the increasing concentrations of nitrogenous species in water streams. Among the nitrogen-containing contaminants, nitrate (NO_3^-) is the most oxidized species and the main pollutant of wastewater.[5] The accumulation of NO_3^- in aquatic systems leads to harmful environmental consequences, such as algal blooms, and the poisoning of fishes and their predators, possibly creating "dead zones".[6] Fertilizers are the main source of nitrogenous contaminants, from which we can establish a clear correlation between NO_3^- contamination in groundwater and rivers with areas in which more agricultural activities are conducted.[7,8] Besides agriculture, some industrial processes have NO_3^- as one of the components of their wastewater.[9] Thus, the accumulation of NO_3^- is an alarming problem that needs to be addressed to restore the disturbed nitrogen cycle. The development of technologies that convert NO_3^- into benign (N_2) or more valuable (NH_3) nitrogenous species is crucial to dealing with this issue.[9–13]

The electrochemical NO_3^- reduction reaction (NO_3RR) to NH_3 is an interesting alternative to overcome the accumulation of nitrate and reduce the high carbon footprint of the Haber–Bosch process, when powered by renewable energy.[5,14–16] Although NO_3^- is not as abundant as N_2, by using a pollutant to produce a valuable fertilizer, we would be managing nitrogenous species toward a circular economy, which could help the reestablishment of the disturbed nitrogen cycle.[15] Nevertheless, NO_3RR to NH_3 is a complex reaction that involves the transfer of eight electrons with many possible byproducts, such as nitrite, nitric oxide, nitrous oxide and hydrazine. The pH of the electrolyte is very important for electrochemical reactions and actively dictates the reaction mechanism of NO_3RR. Liao et al.[17] has recently shown that electrolyte engineering can fundamentally steer NO_3RR selectivity, with a halogen-mediated proton feeding strategy. Additionally, the NO_3RR to NH_3 can either consume 10

---

[a] G. F. Costa, M. E. G. Winkler, M. R. Pinto, R. Nagao
Institute of Chemistry, University of Campinas, Campinas, SP 13083-862, Brazil
E-mail: nagao@unicamp.br

[b] M. E. G. Winkler, R. Nagao
Center for Innovation on New Energies, University of Campinas, Campinas, SP 13083-084, Brazil

[c] F. H. B. Lima
São Carlos Institute of Chemistry, University of São Paulo, São Carlos, SP 13560-970, Brazil

G. F. Costa
Present address: Catalan Institute of Nanoscience and Nanotechnology (ICN2), CSIC and Barcelona Institute of Science and Technology, UAB Campus, Bellaterra, Barcelona 08193, Spain

M. R. Pinto
Present address: Surface Physics and Catalysis (SurfCat), Department of Physics, Technical University of Denmark, Kongens Lyngby 2800, Denmark

Supporting information for this article is available on the WWW under https://doi.org/10.1002/cctc.202501022

moles of protons (Equation 1) or produce 9 moles of hydroxyls (Equation 2) per mole of NH_3 produced depending on the electrolyte pH,[16] which can impact both local[18] and bulk pH during the electrochemical reaction.[19]

$$NO_3{}^-{}_{(aq)} + 10H_3O^+{}_{(aq)} + 8e^- \rightarrow NH_4{}^+{}_{(aq)} + 13H_2O_{(l)} \tag{1}$$

$$NO_3{}^-_{(aq)} + 6H_2O_{(l)} + 8e^- \rightarrow NH_3{}_{(g)} + 9OH^-{}_{(aq)} \tag{2}$$

Examining the steps required to produce NH_3 from NO_3RR, they consist of multiple proton-coupled electron transfer (PCET) steps. In this regard, the concentration of protons can determine whether a hydroxonium cation (H_3O^+) or a water molecule will be the proton source for the NO_3RR. Anionic species can also donate protons to the hydrogenation of the adsorbates, such as hydrogenophosphate, bicarbonate, etc. Depending on the electrolyte pH, the reaction can follow different elementary steps, and the solution pH determines the predominant species from an acid/base equilibrium, depending on its acid dissociation constant (pK_a). For instance, NH_2OH can be protonated to NH_3OH^+ at pHs lower than 5.93.

Cu-based catalysts have compelling attributes that make them a strong candidate to make the electrocatalytic NO_3RR to NH_3 viable. Cu is a cheap and abundant metal that has a favorable charge transfer between its *d*-band and $NO_3{}^-$ LUMO π^* and promotes $NO_{(ads)}$ hydrogenation to $NHO_{(ads)}$ especially, when it is undercoordinated, which favors the formation of NH_3.[20–22] The influence of the pH on single crystals Cu activities for NO_3RR was well studied by Pérez-Gallent et al.[23] They found that at pH 1, HNO_2 is the first intermediate formed, from which NO is released in solution and then re-adsorbed ($NO_{(ads)}$) to be further reduced to $NH_4{}^+$ for both Cu(100) and Cu(111) surfaces. For pH 13, they detected the formation of $NO_2{}^-{}_{(aq)}$ and $NH_2OH_{(ads)}$ on both Cu surfaces, being faster on Cu(100).[23] Hu et al.[24] also explored both pH and Cu facet influences on NO_3RR to NH_3 with density functional theory (DFT) calculations and reported that the rate-limiting step (RLS) and overpotentials are pH-dependent. Although these findings clarify the mechanism at those boundary pHs (1 and 13), the mechanisms underlying NO_3RR at mildly acid and alkaline electrolytes on Cu remain unclear. Understanding how near-neutral pHs impact the NO_3RR is crucial to enable the wastewater treatment of nitrate-rich streams since most of them are neutral solutions.

In this study, we first evaluate through electrochemical experiments how the solution pH from 4.4 to 9.3 impacts the NO_3RR to $NO_2{}^-$. Using *on line* differential electrochemical mass spectrometry (DEMS), we also established a pH influence on the formation of gaseous intermediates and how it dictates the mechanisms that NO_3RR can undergo. We employed in situ Fourier transform infrared (FTIR) spectroscopy to investigate the impact of local pH changes from NO_3RR on Cu at bulk pH 4.4 and 9.3. Our study complements extensive reports on both Cu[19,23,25] and Cu-based catalysts[19,26–29] under various electrolyte conditions, where the focus has been primarily on products distributions toward ammonia and nitrite. We concentrate on the intermediate chemistry and pH-dependent interfacial processes, which are key to rationalizing why different electrolytes lead to distinct products selectivity.[30] Thus, we could provide a picture of how near-neutral pHs ranging from 4.4 to 9.3 dictate the NO_3RR mechanisms on metallic Cu to elucidate crucial aspects of designing electrolytes for this reaction.

2. Experimental Methods

2.1. Electrochemical Measurements

We conducted potentiostatic chronoamperometric experiments in a two-compartment electrochemical cell separated by a Nafion 424 membrane. We used a saturated Ag/AgCl reference electrode (RE), a Pt plate as a counter electrode (CE), and a previously electropolished Cu mesh (Alfa Aesar, copper gauze, 50 mesh woven from 0.23 mm diameter wire) as working electrode (WE). The electropolishing protocol consisted of applying +3.0 V versus Cu at the WE for 30 s using a 50% H_3PO_4 solution followed by the application of 0.0 V versus Cu for another 30 s. We applied potentials from −0.1 to −0.8 V versus standard hydrogen electrode (SHE) for 60 s for each measurement to obtain the steady-state current at each condition. At pH 9.3, we also did measurements at potentials –0.9 and –1.0 V versus SHE. The potentials were applied using a previously calibrated saturated Ag/AgCl reference electrode (with the potential against SHE at pH 0 denoted as $E^0{}_{Ag/AgCl}$) and were corrected versus SHE and reversible hydrogen electrode (RHE) according to the following Equations (3 and 4) respectively:

$$E_{SHE} = E_{Ag/AgCl} + E^0_{Ag/AgCl} \tag{3}$$

$$E_{RHE} = E_{Ag/AgCl} + E^0_{Ag/AgCl} + 0.059\text{ V pH} \tag{4}$$

The electrolyte consisted of 0.2 mol L^{-1} $Na_xH_{3-x}PO_4$ varying the quantities of NaH_2PO_4 (sodium phosphate monobasic dihydrate > 98%, Sigma-Aldrich) or Na_2HPO_4 (sodium phosphate dibasic heptahydrate > 98%, Sigma-Aldrich) to obtain solution pHs of 4.4, 7.1, and 9.3, with and without the addition of 0.05 mol L^{-1} $NaNO_2$ or $NaNO_3$ (>99%, Sigma-Aldrich) in the catholyte. Argon was purged before (at least for 15 min) and during the electrolysis. The catholyte was stirred at 700 rpm to minimize the current limitation by mass transport. All electrolysis measurements were 85%-*iR*-compensated considering the impedance measured at 100 kHz at open circuit potential (OCP), with the remaining 15% *iR* being considered afterward for data analysis. The pHs were measured after the experiments and did not change significantly. We calculated the electrochemically active surface area (ECSA) of the Cu mesh through the measurement of the double layer capacitance (C_{dl}). By varying the scan rate and extracting the slope of the relationship between the capacitive current and scan rate, we can obtain the C_{dl} and we are able to get the ECSA by the ratio between C_{dl} and the specific capacitance (C_s) of Cu, which we considered to be 34 μF cm^{-2}.[19] We show in Figure S1 the CVs and the calculation of C_{dl} for the Cu mesh at pH 7.1.

2.2. *On Line* Differential Electrochemical Mass Spectrometry

We performed *on line* DEMS experiments to track the variation of the ionic current (I_{ionic}) of key mass/charge ratios (*m/z*) during electrochemical experiments. The DEMS equipment consists of a mass spectrometer with a vacuum system, powered by two turbomolecular pumps operating at 60,000 rpm (HIPACE 300 Turbopump DN 100 CF-F) and a mechanical pre-vacuum pump, two chambers, and valves.[31,32] We used a DEMS with two chambers that under operating conditions with a difference of pressure of up to 4 orders of magnitude (each one with a pressure in the order of 10^{-3} and 10^{-7} hPa). This pressure difference enables the differential detection of the gaseous and volatile species.[31] The mass spectrometer (PrismaPlus QMG 220 M1) is located in the second chamber and consists of a tungsten filament that ionizes the gaseous collected species that are detected by a secondary electron multiplier detector. We acquired potentiostatic chronoamperometric steps of 120 s each from −1.4 to −1.7 V versus SHE in duplicates. Between each step (120 s) and during the whole DEMS session, a potential of −0.7 V versus SHE was kept in an electrochemical cell to maintain Cu in its metallic state, considering Cu can be oxidized at OCP. We monitored the I_{ionic} of *m/z* 5, 30, 32, 33, and 44. The *m/z* 5 is monitored to verify if the baseline of all *m/z* is not being affected by differences in the pressure of the chamber, which was not the case. The I_{ionic} for each monitored *m/z* is normalized, considering the stabilized baseline of each series of chronoamperometric experiments. The WE consisted of a copper mesh (Alfa Aesar, copper gauze, 50 mesh woven from 0.23 mm diameter wire) positioned above a titanium ring that serves as electrical contact. This assembly is secured in a Teflon support beneath four poly(tetrafluoroethylene) (PTFE) membranes (Gore-Tex, 0.02 µm pore size, 50 µm thickness), which act as the interface between the electrochemical cell and the vacuum chambers of the DEMS setup. On this assembly, a stainless-steel flange (with a frit of 40 µm pore size) is screwed onto the PTFE membranes (Figure S2a,b), which is connected to the DEMS chambers. The exposed geometric area was 0.38 cm^2. We used a custom-made electrochemical cell with a Pt plate as CE and a leakless Ag/AgCl as RE, under magnetic stirring at 700 rpm and Ar atmosphere. The electrolyte consisted of 0.2 mol L^{-1} NaH_2PO_4 or Na_2HPO_4 for pHs 4.4 or 9.3, respectively, with the addition of 0.1 mol L^{-1} $NaNO_3$. The pHs were measured after the experiments and did not change significantly.

2.3. In Situ Fourier Transform Infrared Spectroscopy

The spectroelectrochemical cell used for in situ FTIR experiments consists of a 3-electrode cell (WE = Cu mesh; CE = Pt wire; RE = Ag/AgCl) that was assembled on top of a ZnSe window and positioned on the upper part of a 6-reflection attenuated total reflectance (ATR) accessory (Specac Gateway multi-reflection HATR) mounted in a Nexus 670 ThermoNicolet spectrometer (Figure S3). The FTIR spectra were acquired in ATR mode from a thin layer formed by the careful pressure of the WE against the ZnSe window by the sample holder. We used a PGSTAT 204 potentiostat (Autolab) to conduct chronoamperometric experiments from −0.4 to −1.1 V versus SHE (at every 100 mV). We acquired the spectra from an average of 16 scans and 8 cm^{-1} resolution. The background spectra were obtained at −0.4 V versus SHE. Positive peaks correspond to the formation of products and/or the adsorption of species, while valleys are associated with the consumption of species and/or their displacement from the surface.

3. Results and Discussion

3.1. The Influence of pH on the Rate-Limiting Step of Nitrate Electrocatalytic Reduction on Copper

We evaluated the pH influence on Cu intrinsic activity for NO_3RR and nitrite (NO_2^-) reduction (NO_2RR) by employing chronoamperometric experiments. In Figure 1, we show the comparison of the steady-state cathodic current density of a Cu mesh from −0.1 to −1.0 V versus SHE for hydrogen evolution reaction (HER) with the electrolyte containing only $Na_xH_{3-x}PO_4$, NO_3RR, and NO_2RR at different pHs (4.4, 7.1, and 9.3). We show in Figure S4 representative chronoamperometric measurements at all pHs. For NO_3RR and NO_2RR, we evaluate the steady-state overall current in the presence of 0.05 mol L^{-1} $NaNO_x$, which means that some activity is still related to the competing HER. Considering we cannot assume that HER will occur at the same rates in the presence of NO_3^- or NO_2^-, we did not merely subtract the HER current density in the absence of these anions from the overall current obtained in their presence. Even so, we could extract some elucidative trends that will be explored as follows.

We compare the cathodic current densities of Cu at pHs 4.4 (blue lines), 7.1 (green lines) and 9.3 (red lines) in the absence (Figure 1a,d) and presence of NO_2^- (Figure 1b,e) and NO_3^- (Figure 1c,f). Considering the reactions are all proton-consuming, all of them should reflect decreasing activity with increasing pH when comparing the current densities in the SHE scale (Figure 1a–c). This trend is valid for both HER (Figure 1a) and NO_2RR (Figure 1b), where we see that by increasing the pH, we lower their associated current densities. When we exclude the influence of proton concentration by comparing the activities of HER, NO_2RR in the RHE scale (Figure 1d,e), we observe that the current densities are similar for all pHs, indicating that the kinetics of these reactions are dictated by PCET processes.[33] For a better understanding of changing scales, we show in Table S2 the correlation between the applied potential at SHE and RHE at different pHs, highlighting that a fixed potential at SHE scale corresponds to increasingly positive values at RHE scale with rising the pH.

A pH-dependence of Cu activities for NO_3RR on SHE scale (Figure 1c) is not evident as they present similar profiles for pHs 4.4 and 7.1, which means that the reaction rate is not governed by a proton-electron transfer, since it is not pH-sensitive.[33] By disregarding the influence of the protons' concentration (RHE scale), the NO_3RR (Figure 1f) is more favorable at pH 7.1. This observation can be explained by the fact that the mechanism of

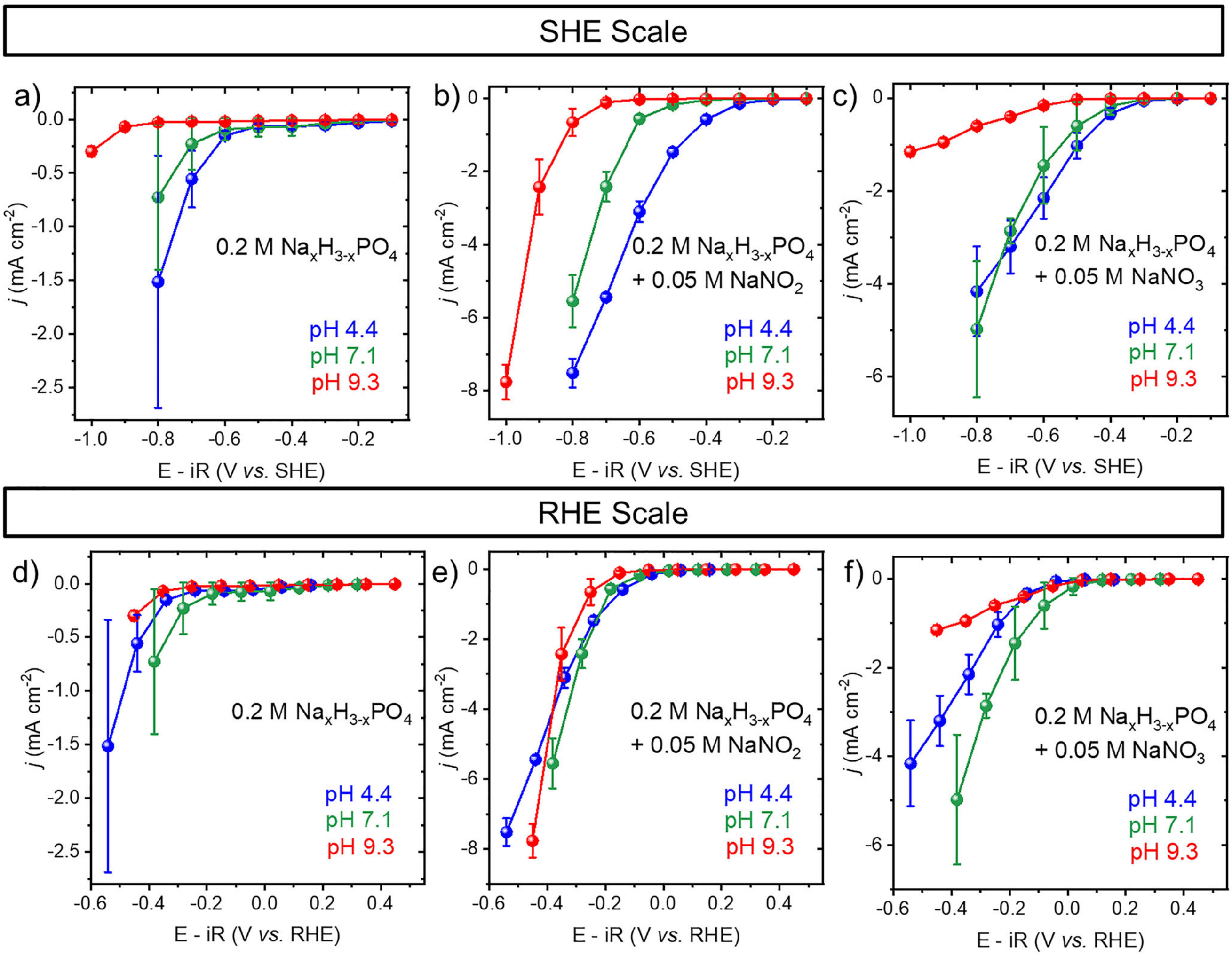

Figure 1. Potential dependence on SHE a)–c) and RHE d)–f) scales of the steady-state current of 1-min chronoamperometric experiments conducted in different electrolytes using a copper mesh as the working electrode. pH influence on the activity of Cu for the electrolyte containing 0.2 mol L^{-1} $Na_xH_{3-x}PO_4$ with the absence a) and d) and presence of 0.05 mol L^{-1} $NaNO_3$ b) and e) or 0.05 mol L^{-1} $NaNO_2$ c) and f). The experiments were conducted in a 2-compartment H-cell separated by a Nafion 424 membrane, using a previously electropolished Cu mesh as the working electrode, saturated Ag/AgCl reference electrode, and a Pt plate as counter electrode under Ar atmosphere. The catholyte was stirred at 700 rpm to avoid mass transport limitation of the recorded currents. The error bars denote the standard deviation of three separate experiments.

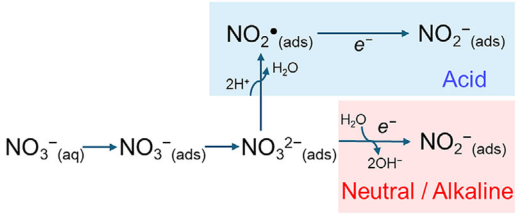

Scheme 1. Reaction mechanisms through which the nitrate reduction to nitrite can occur depending on the pH: acidic one highlighted in blue and neutral/alkaline one highlighted in red.

the rate-limiting step (RLS) for NO_3RR (NO_3^- adsorption and its reduction to NO_2^-) depends on the pH, which involves a direct proton transfer in mildly acidic electrolyte, followed by the electron transfer to form adsorbed NO_2^-. Scheme 1 shows different paths through which NO_3RR to $NO_2^-{}_{(ads)}$ can undergo depending on the pH.

Considering the proposed mechanisms in Scheme 1,[14] along with our results, we attribute the acidic RLS for pH 4.4 and the neutral/alkaline RLS for pHs 7.1 and 9.3. We consider that the neutral/alkaline path would be the predominant one for pH 7.1 since the activities of Cu for NO_3RR are different compared to pH 4.4 at the RHE scale (Figure 1f), which indicates that the reaction rates are not dominated by the concentration of protons and does not involve a PCET step as RLS. By shifting the reaction mechanism from one that consumes protons (acid path) to another one that consumes H_2O molecules (neutral/alkaline) producing hydroxyl (OH^-), comparing only the pHs 7.1 and 9.3, the reaction is more favorable at pH 7.1. Enhanced activity at pH 7.1 compared to 9.3 likely arises from more favorable reaction thermodynamics and interfacial conditions. At pH 7.1, the buffering capacity allows for moderate proton availability without the inhibitory accumulation of hydroxide, enabling a more balanced environment for PCET-driven reduction steps. Although the initial reduction of NO_3^- yields NO_2^-, the ultimate objective of NO_3RR is the conver-

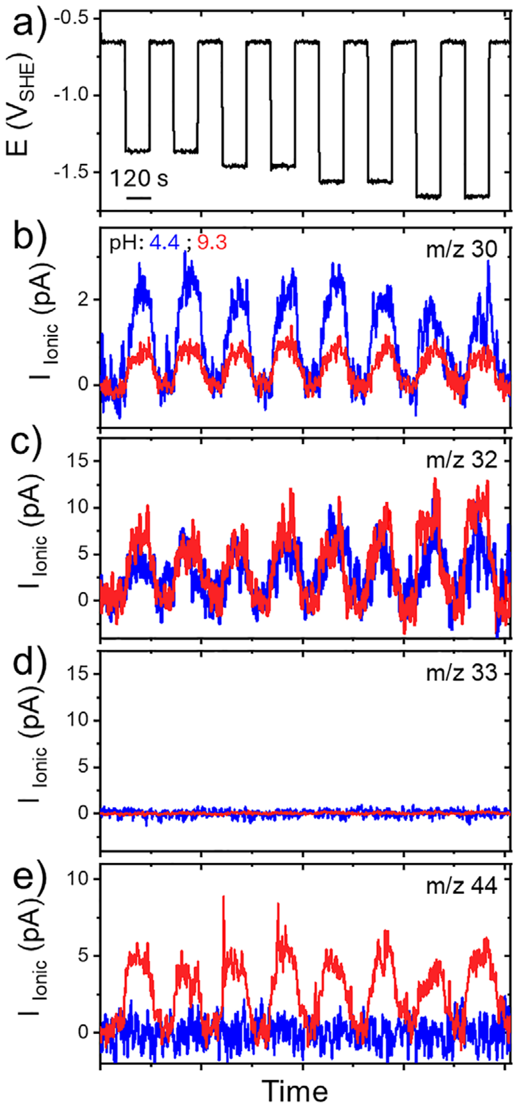

Figure 2. DEMS results for the production of nitric oxide. a) Potential steps applied over time. Variation of ionic current related to $m/z = 30$ b), 32 c), 33 d), and 44 e) for nitrate electrochemical reduction on Cu at pHs 4.4 (blue line) and 9.3 (red line). Experiments were conducted in a 1-compartment electrochemical cell containing 0.2 mol L^{-1} of NaH_2PO_4 (pH 4.4) or Na_2HPO_4 (pH 9.3) + 0.1 mol L^{-1} $NaNO_3$, a Cu mesh as working electrode, Pt as counter electrode and a leak-free Ag/AgCl as reference electrode.

sion into environmentally benign nitrogen species, such as N_2, or valuable ones, such as NH_3. In the following subsection, we discuss the effect of pH in the next steps of NO_3RR on Cu.

3.2. The pH-Dependent Formation and Hydrogenation of Nitric Oxide

On line DEMS (Figure 2) measurements were conducted to track the formation of volatile species formed from NO_3RR on Cu electrode at pHs 4.4 (blue line in Figure 2b–e) and 9.3 (red line in Figure 2b–e) by monitoring the variation of the ionic current (I_{ionic}) related to their mass charge ratio (*m/z*). We present in Figure 2a the steps of potential (120 s each) employed to qualitatively detect the potential-dependent production of: NO ($m/z = 30$, Figure 2b), N_2H_4 ($m/z = 32$, Figure 2c), NH_2OH ($m/z = 33$ and 32–$NHOH^+$ fragment–Figure 2c,d) and N_2O ($m/z = 44$ and 30–NO^+ fragment – Figure 2b,e). We alterneted potentials between values at which an increase in I_{ionic} was observed (from −1.4 to −1.7 V versus SHE) and −0.7 V, which lies in the double-layer region, where no faradaic current or increase in the I_{ionic} is detected. This approach allowed the I_{ionic} to return to the baseline level between steps. We applied sufficiently negative potential to produce a detectable number of volatile species, but it may not reflect the actual potential from which we start to produce them. Our goal is to show the potential dependence of the production of each species from NO_3RR on Cu at different pHs (4.4 and 9.3).

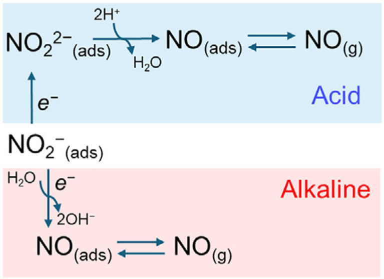

Scheme 2. Reaction mechanisms for nitrite conversion to NO at acidic (blue) and alkaline (red) pHs.

The formation of NO was tracked by examining the variation of I_{ionic} of $m/z = 30$ (Figure 3b), which is a central intermediate of NO_3RR after the reduction of $NO_2^-{}_{(ads)}$. We observe a potential-dependent increase of the I_{ionic} of $m/z = 30$ at both pH 4.4 and pH 9.3. The ionization of N_2O can generate fragment NO^+ with *m/z* 30 with up to one third of the intensity of the main fragment with *m/z* 44. Thus, since the variation in I_{ionic} of *m/z* 30 (Figure 2b) represents one-fifth of the variation of *m/z* 44 (Figure 2e) at pH 9.3, we cannot state that the variation of *m/z* 30 under alkaline conditions is attributed to NO formation. Therefore, we can conclude that the reduction of NO_2^- to NO is more favorable at pH 4.4, which corroborates with our previous result for the reduction of nitrite (Figure 1b), and with what was found by Perez-Gallent et al. at single crystal Cu at pH 1 compared to pH 13.[23] It is important to note that the variation of $m/z = 30$ may also be assigned to the production of N_2O, as NO^+ is a known fragment of nitrous oxide.[34] However, since we just detected N_2O at pH 9.3 (Figure 2e), the stronger variation of $m/z = 30$ signal observed at pH 4.4 is more likely attributed to increased NO production. The $NO_2^-{}_{(ads)}$ reduction to NO can undergo through different pathways, depending on the electrolyte pH, as presented in Scheme 2.[14]

The $NO_2^-{}_{(ads)}$ species can be reduced to $NO_{(ads)}$, consuming one electron.[5] The formation of $NO_{(ads)}$ can undergo through an electron transfer that forms $NO_2^{2-}{}_{(ads)}$ followed by the reaction with two protons releasing H_2O in acidic media (highlighted in blue in Scheme 2). In alkaline media, $NO_{(ads)}$ is formed through the consumption of one H_2O molecule and one electron transfer (alkaline mechanism, in red).[5,14] The higher concentration of protons under acidic conditions would favor the equilibrium

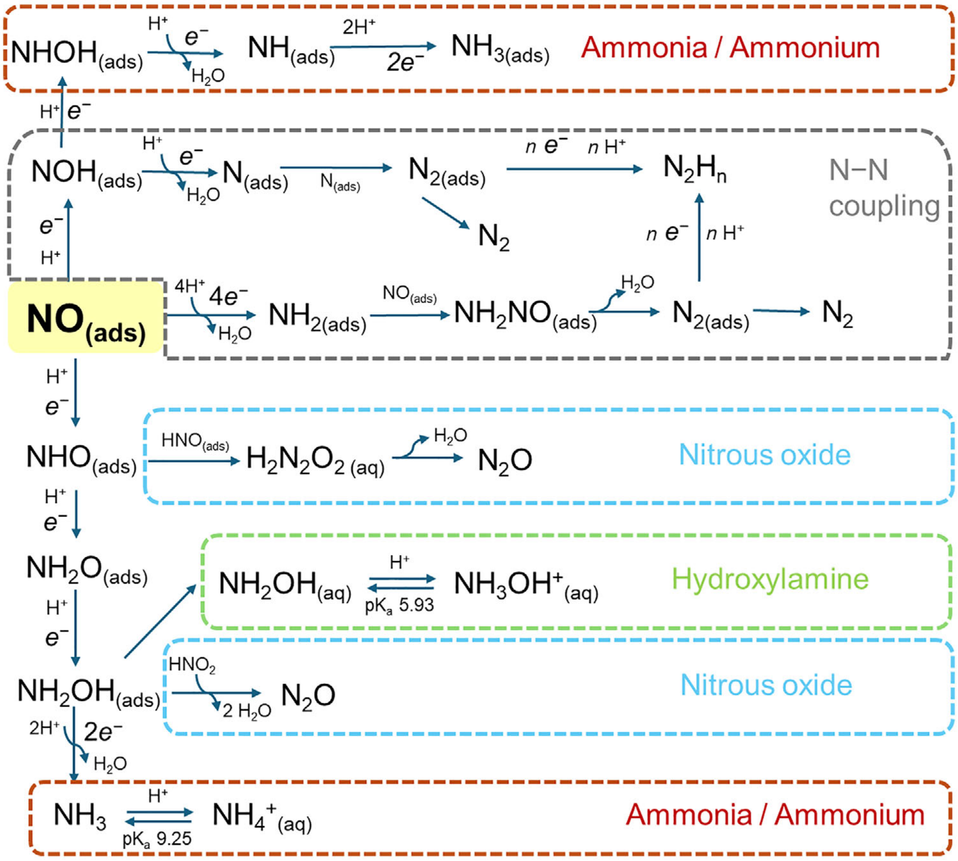

Scheme 3. Reduction of adsorbed NO to the formation of different products: N-N coupling in gray, nitrous oxide in light blue, hydroxylamine in green and ammonia/ammonium in red.

toward NO formation, in accordance with what we observed with DEMS (Figure 2b). Another important factor to consider is the difference in concentration of cations between the electrolytes (Table S1). At pH 9.3, the Na^+ concentration is 0.4 mol L^{-1}, whereas at pH 4.4, it is 0.2 mol L^{-1}. A higher concentration of cations enhances the stabilization of adsorbates with a dipole moment,[30,35] which may explain the increased detection of $NO_{(g)}$ species at lower pH. Thus, at pH 4.4, the lower concentration of cations provides less stabilization for this adsorbate, favoring its desorption and detection with DEMS.

After the formation of $NO_{(ads)}$, numerous other products can be produced, as shown in Scheme 3. By utilizing DEMS, we can monitor the formation of potential gaseous and volatile species, providing insights into the reaction pathways and product distribution. Scheme 3 shows the different paths through which NO_3RR can undergo from the divergent central intermediate $NO_{(ads)}$. The protonation of NO dictates the selectivity of NO_3RR, which can be either through N atom or O atom.[36] By favoring the formation of the intermediate $NOH_{(ads),}$ the N–N coupling mechanisms (highlighted in gray in Scheme 3) are more likely to occur,[21,37,38] promoting the formation of N_2. We can also obtain NH_3 from $NOH_{(ads)}$ through its subsequent protonation at the N atom to form $HNOH_{(ads)}$ followed by the release of water to form $NH_{(ads)}$ species (highlighted in red on the top of Scheme 3). This mechanism for NH_3 is less likely to occur than N_2 formation since it demands three additional PCET steps to obtain NH_3 compared to N_2.[14] From the formation of $NHO_{(ads)}$, especially for what is reported for Cu-based catalysts,[23,39,40] the production of hydroxylamine (NH_2OH) (highlighted in light green in Scheme 3) and NH_3 (highlighted in red at the bottom of Scheme 3) is more favorable. Katsounaros and Kyriacou[41] reported two possible mechanisms for the formation of nitrous oxide (N_2O) either through the coupling of two $HNO_{(ads)}$ species or from the reaction between $H_2NOH_{(ads)}$ with $HNO_{2(aq)}$ (highlighted in light blue in Scheme 3). Once formed, N_2O can be either desorbed – as we detected with DEMS – or further reduced.[5]

We monitored the formation of N_2H_4 ($m/z = 32$, Figure 2c), NH_2OH ($m/z = 32$ and 33, Figure 2c,d), N_2O ($m/z = 44$, Figure 2e) with the applied potential (Figure 2a). The $m/z = 32$ can be attributed to hydrazine (N_2H_4)[34] and to a fragment of hydroxylamine (NH_2OH), whose main molecular fragment has $m/z = 33$.[42] NH_2OH can be protonated to NH_3OH^+ at acidic pH with a pK_a equal to 5.93 (highlighted in green in Scheme 3), which means that for pH = 4.4 we would not expect to have considerable amounts of NH_2OH in solution. We found a potential-dependent variation of I_{ionic} of $m/z = 32$ (Figure 2c) for both pHs, which could be attributed to both N_2H_4 and NH_2OH. However, considering that $m/z = 33$ (Figure 2d) does not vary at the same scale, and NH_2OH is not expected to be present in solution at pH 4.4 ($pK_a = 5.93$),[14] we attribute this variation to the formation of N_2H_4 through the protonation of $^*N_2$ adsorbed species, as shown in Scheme 3, highlighted in gray.[38] Although

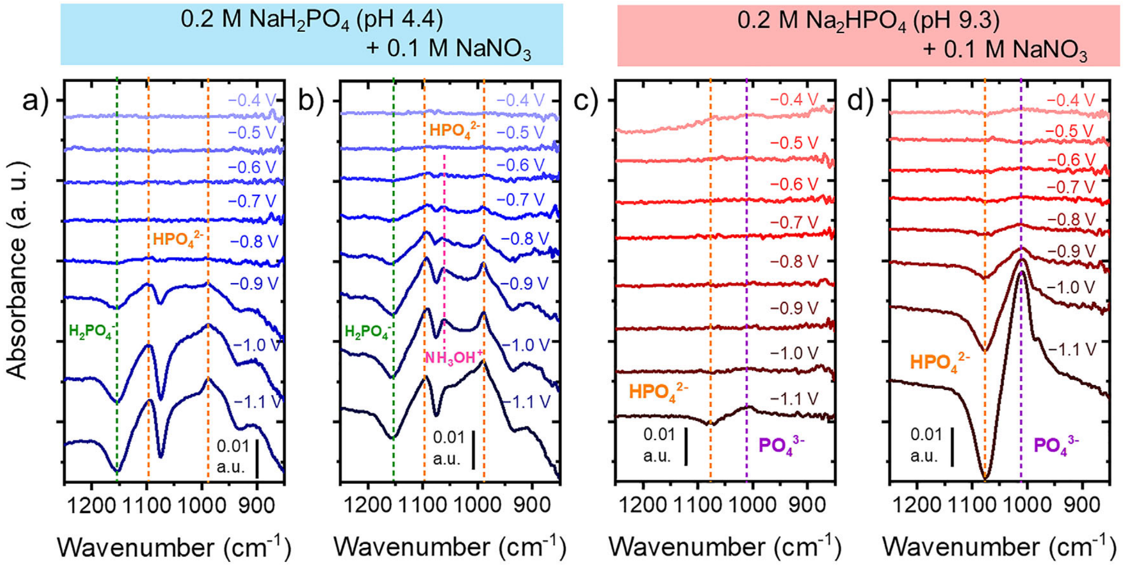

Figure 3. In situ Fourier transform infrared spectra for nitrate reduction on Cu at different pHs. Experiments were conducted under potentiostatic regime in a 1-compartment electrochemical cell containing 0.2 mol L^{-1} of NaH$_2$PO$_4$ (pH 4.4) a) and b) or Na$_2$HPO$_4$ (pH 9.3) c) and d) + 0.1 mol L^{-1} NaNO$_3$ b) and d), a Cu mesh as working electrode, Pt as counter electrode and a leak-less Ag/AgCl as reference electrode. The potentials are represented by shades of blue (pH 4.4) or red (pH 9.3) and were corrected against SHE. Peaks and valleys attributed to the species H$_2$PO$_4^-$, HPO$_4^{2-}$, PO$_4^{3-}$ and NH$_3$OH$^+$ are highlighted with green, orange, purple, and pink dotted lines, respectively. The spectra were acquired after 3 min of chronoamperometry at each applied potential.

we do not attribute the variation of $m/z = 32$ to NH$_2$OH, we cannot state that it is not being formed during NO$_3$RR, as it is a liquid soluble species with low volatility,[43] and would be protonated at pH 4.4 considering its pK_a of 5.93.[5] Besides that, we will discuss in the next subsection the formation of NH$_3$OH$^+$, the protonated form of hydroxylamine at pH 4.4, probed by in situ FTIR.

N$_2$O can be formed through two different pathways (highlighted in light blue in Scheme 3): by the coupling of two species HNO$_{(ads)}$ during NO$_3$RR leading to the formation of H$_2$N$_2$O$_2$ which dissociates releasing N$_2$O and H$_2$O and through the reaction of H$_2$NOH$_{(ads)}$ with HNO$_{2(aq)}$, as reported by Katsounaros and Kyriacou.[41] We tracked the formation of N$_2$O by probing the I$_{ionic}$ related to $m/z = 44$ (Figure 2e). We found a potential-dependent formation of N$_2$O only for pH 9.3, which was not observed for pH 4.4. We attribute this side mechanism occurring at a more alkaline pH to the fact that HNO$_{(ads)}$ would be rapidly protonated to form H$_2$NO$_{(ads)}$ at pH 4.4, inhibiting the formation of N$_2$O under this condition. We do not expect the formation of N$_2$O through the second mechanism (HNO$_2$-mediated one) considering that the pK_a of HNO$_2$ is equal to 3.4,[5] and therefore it is not expected be present in solution at both studied pHs.

3.3. The Effect of Nitrate Reduction on Local pH Alkalinization

Although the bulk pH can be kept constant by using buffered solutions, the interfacial pH can vary under reduction reaction conditions by the local consumption of protons.[44] It can lead to a pH gradient between the WE and the bulk of the electrolyte,[45] which is the critical region where the electrochemical reaction occurs. Corson et al.[18] reported the use of attenuated total reflectance-surface-enhanced infrared spectroscopy (ATR-SEIRAS) to probe the local pH of the interface between Cu and the electrolyte, which consisted of a phosphate buffer system, for NO$_3$RR. They used the intensities of the peaks from the ATR-SEIRAS spectra attributed to H$_3$PO$_4$, H$_2$PO$_4^-$, HPO$_4^{2-}$ and PO$_4^{3-}$ to determine the local pH during NO$_3$RR.

Our experimental configuration for in situ FTIR (Figure S3) allows the accumulation of produced species at the electrocatalyst surface, effectively retaining them in the local environment that is probed at each spectral acquisition. This approach differs from what we observed using DEMS, where volatile or desorbed species are rapidly transported away from the electrode.[32] Despite probing different phenomena, we believe that these results are complementary. While DEMS provides insights into transient and desorbed intermediates, in situ FTIR captures interfacial dynamics more closely, particularly regarding local pH variations and adsorbed species. By analysing the spectral features of phosphate species in situ, we gain valuable information about the local reaction environment and how it evolves during NO$_3$RR. In this subsection, we investigated qualitatively the dynamics of the peaks attributed to the anions H$_2$PO$_4^-$, HPO$_4^{2-}$ and PO$_4^{3-}$ at pHs 4.4 (Figure 3a,b) and 9.3 (Figure 3c,d) using in situ FTIR in the absence (Figure 3a,c) and presence of 0.1 mol L^{-1} NaNO$_3$ (Figure 3b,d).

The local pH variations at pH 4.4 (Figure 3a,b) are reflected by the decrease in the concentration of H$_2$PO$_4^-$ and the increasing concentration of HPO$_4^{2-}$. These phenomena are observed because lowering the concentration of H$_3$O$^+$ shifts the following equilibrium (Equation 5) toward the direct reaction:

$$H_2PO^-_{4\ (aq)} + H_2O_{(l)} \rightleftharpoons HPO^{2-}_{4\ (aq)} + H_3O^+_{(aq)} \tag{5}$$

We observe this phenomenon for both HER (Figure 3a) and NO$_3$RR (Figure 3b) since both reactions are proton-consuming, leading to local pH alkalinization. We monitored the emergence of a valley at 1155 cm^{-1} (green dotted line, Figure 3a,b) assigned to the asymmetric vibration ν_a (PO) of $H_2PO_4^-$ and the evolution of peaks at 989 and 1093 cm^{-1} assigned to symmetric ν_s (PO) and asymmetric ν_a (PO) vibrations of HPO_4^{2-}, respectively (orange dotted lines, Figures 3a,b).[18] The local pH alkalinization was observed at a low overpotential (–0.6 V versus SHE) when NO_3RR takes place (Figure 3b). The multiple PCET steps involved in the NO_3RR reaction led to a reduced availability of protons within the thin layer probed by FTIR. Additionally, we observed the emergence of a peak at 1060 cm^{-1} only for NO_3RR at pH 4.4 (pink dotted line, Figure 3b), which we attribute to the –NH_2 stretch of $NH_3OH^+_{(aq)}$,[19] considering the equilibrium of hydroxylamine showed in green in Scheme 3.

At pH 9.3 (Figure 3c,d), the local pH alkalinization is reflected by the consumption of HPO_4^{2-} and production of PO_4^{3-}, considering the shift of the equilibrium represented by Equation (6):

$$HPO_{4\,(aq)}^{2-} + OH^-_{(aq)} \rightleftharpoons PO_{4\,(aq)}^{3-} + H_2O_{(l)} \tag{6}$$

A pH alkalinization in both HER (Figure 3c) and NO_3RR (Figure 3d) was observed using in situ FTIR, through which we ascribe the valley at 1076 cm^{-1} to the asymmetric ν_a (PO) vibrations of HPO_4^{2-} (orange dotted lines, Figure 3c,d) and the peak at 1008 cm^{-1} to the ν_a (PO) vibrations of PO_4^{3-} (purple dotted lines, Figure 3c,d).[18] We also observe that the decrease in the concentration of HPO_4^{2-} and the increase in the concentration of PO_4^{3-} occur simultaneously and with similar magnitude for both HER and NO_3RR, reflecting the equilibrium of Equation (6). Additionally, the intensity of the peaks and valleys for NO_3RR (Figure 3d) are higher than those for only HER (Figure 3c) as well as the overpotential from which we started detecting this phenomenon (–0.8 V versus SHE for NO_3RR and –1.1 V versus SHE for HER).

4. Conclusion

We reported an experimental approach to investigate the reaction mechanisms of NO_3RR on metallic Cu depending on the electrolyte pH from 4.4 to 9.3. By comparing the electrochemical results obtained from HER, NO_2RR, and NO_3RR, we could establish the pH influence on the first steps of the NO_3RR to NO_2^-. Our results indicate that NO_3^- be converted into NO_2^- can via two distinct, pH-dependent electrochemical pathways on Cu. We also employed *on line* DEMS to unveil how the electrolyte pH can modulate the product distribution from NO_3RR on Cu, by tracking some key gaseous and volatile species. We found that $NO_{(ads)}$ is preferably formed at pH 4.4. At pH 9.3 side products such as N_2O and N_2H_x can also be formed, due to the lower concentration of protons that promotes the hydrogenation of oxygenated intermediates. Using in situ FTIR spectroscopy, we demonstrated that the NO_3RR favors the local pH alkalinization by consuming protons that shift the equilibria of phosphate anions. The results presented in this work can stimulate the use of coupled techniques to investigate electrolyte conditions for electrochemical reactions by shedding light on the role of mild pH conditions on NO_3RR on Cu electrodes. We highlight that electrolyte engineering is crucial to enable the use of electrochemical alternatives to both wastewater treatment and NH_3 synthesis.

Author Contributions

G.F.C.: Conceptualization; conduction of electrochemical; DEMS and FTIR experiments; data analysis; writing—original draft. **M.E.G.W.**: Conduction of FTIR experiments; DEMS and FTIR data interpretation; writing—review and editing. **M.R.P.**: Electrochemical experiments; DEMS and FTIR data interpretation; writing—review and editing. **F.H.B.L.**: DEMS and FTIR data interpretations; writing—review and editing. **R.N.**: Conceptualization; funding acquisition; supervision; writing—review and editing.

Acknowledgments

The authors acknowledge support from Fundação de Amparo à Pesquisa do Estado de São Paulo (FAPESP) process numbers: G.F.C. 2019/18847–6; M.E.G.W. 2023/10045–3; M.R.P. 2019/08244–2; F.H.B.L. 2019/22183–6; R.N. 2023/02841–4 and 2024/03807–7; and Conselho Nacional de Desenvolvimento Científico e Tecnológico (CNPq) process numbers: M.E.G.W. 151227/2023–3; F.H.B.L. 308948/2022–0 and 406933/2021–9; R.N. 421313/2023–4. F.H.B.L. acknowledges RCGI (Research Centre for Greenhouse Gas Innovation) hosted by the University of Sao Paulo (USP) and sponsored by FAPESP 2014/50279–4 and 2020/15230–5; R.N. acknowledge CINE (Center for Innovation on New Energies) hosted by the University of Campinas (UNICAMP) and sponsored by FAPESP 2017/11986–5; F.H.B.L. and R.N. acknowledge Shell Brazil and the strategic importance of the support given by ANP - Brazil's National Oil, Natural Gas and Biofuels Agency, through the R&D levy regulation. We thank Matheus Sales and Kauan Gomes for their contributions to extra experimental investigations related to this work.

The Article Processing Charge for the publication of this research was funded by the Coordenação de Aperfeiçoamento de Pessoal de Nível Superior - Brasil (CAPES) (ROR identifier: 00x0ma614).

Conflict of Interests

The authors declare no conflict of interest.

Data Availability Statement

The data that support the findings of this study are available from the corresponding author upon reasonable request.

Keywords: Ammonia synthesis · Electrocatalysis · Electrochemistry · Nitrate reduction · Nitrogen cycle · pH effect

[1] M. A. Sutton, D. Simpson, P. E. Levy, R. I. Smith, S. Reis, M. van Oijen, W. de Vries, *Glob. Chang. Biol.* **2008**, *14*, 2057–2063.
[2] J. M. Melillo, *Ambio* **2021**, *50*, 759–763.
[3] S. Fields, *Environ. Health Perspect.* **2004**, *112*, A556–A563.
[4] National Academy of Engineering, National Academy of Engineering Grand Challenges For Engineers, **2017**.
[5] S. Garcia-Segura, M. Lanzarini-Lopes, K. Hristovski, P. Westerhoff, *Appl. Catal. B* **2018**, *236*, 546–568.
[6] I. Bogárdi, R. D. Kuzelka, *Nitrate Contamination* (Ed: W. G. Ennenga), Springer, Berlin Heidelberg, Berlin, Heidelberg **1991**.
[7] A. H. Mahvi, J. Nouri, A. A. Babaei, R. Nabizadeh, *Int. J. Environ. Sci. Technol.* **2005**, *2*, 41–47.
[8] J. F. Power, J. S. Schepers, *Agric. Ecosyst. Environ.* **1989**, *26*, 165–187.
[9] P. H. van Langevelde, I. Katsounaros, M. T. M. Koper, *Joule* **2021**, *5*, 290–294.
[10] I. Katsounaros. *Curr. Opin. Electrochem.* **2021**, *28*, 100721.
[11] Y. Zeng, C. Priest, G. Wang, G. Wu, *Small Methods* **2020**, *4*, 2000672.
[12] N. Gruber, J. N. Galloway, *Nature* **2008**, *451*, 293–296.
[13] J. N. Galloway, J. D. Aber, J. W. Erisman, S. P. Seitzinger, R. W. Howarth, E. B. Cowling, B. J. Cosby, *Bioscience* **2003**, *53*, 341–356.
[14] D. Anastasiadou, Y. van Beek, E. J. M. Hensen, M. C. Figueiredo, *Electrochem. Sci. Adv.* **2022**, *3*, e2100220.
[15] N. Singh, B. R. Goldsmith, *ACS Catal.* **2020**, *10*, 3365–3371.
[16] Z. Wang, D. Richards, N. Singh, *Catal. Sci. Technol.* **2021**, *11*, 705.
[17] W. Liao, J. Wang, G. Ni, K. Liu, C. Liu, S. Chen, Q. Wang, Y. Chen, T. Luo, X. Wang, Y. Wang, W. Li, T.-S. Chan, C. Ma, H. Li, Y. Liang, W. Liu, J. Fu, B. Xi, M. Liu, *Nat. Commun.* **2024**, *15*, 1264.
[18] E. R. Corson, J. Guo, W. A. Tarpeh, *J. Electrochem. Soc.* **2024**, *171*, 046503.
[19] G. F. Costa, M. Winkler, T. Mariano, M. R. Pinto, I. Messias, J. B. Souza, I. T. Neckel, M. F. C. Santos, C. F. Tormena, N. Singh, R. Nagao, *Chem Catal.* **2024**, *4*, 100850.
[20] T. Hu, M. Wang, L. Ren, C. M. Li, C. Guo, *J. Phys. Chem. Lett.* **2024**, *15*, 3258–3266.
[21] E. Romeo, M. F. Lezana-Muralles, F. Illas, F. Calle-Vallejo, *ACS Appl. Mater. Interfaces* **2023**, *15*, 22176–22183.
[22] A. S. Fajardo, P. Westerhoff, C. M. Sanchez-Sanchez, S. Garcia-Segura, *Appl. Catal. B* **2021**, *281*, 119465.
[23] E. Pérez-Gallent, M. C. Figueiredo, I. Katsounaros, M. T. M. Koper, *Electrochim. Acta* **2017**, *227*, 77–84.
[24] T. Hu, C. Wang, M. Wang, C. M. Li, C. Guo, *ACS Catal.* **2021**, *11*, 14417–14427.
[25] O. Q. Carvalho, R. Marks, H. K. K. Nguyen, M. E. Vitale-Sullivan, S. C. Martinez, L. Árnadóttir, K. A. Stoerzinger, *J. Am. Chem. Soc.* **2022**, *144*, 14809–14818.
[26] I. Messias, M. R. Pinto, A. C. Roveda, A. C. Queiroz, F. H. B. Lima, R. Nagao, *Electrochim. Acta* **2022**, *436*, 141445.
[27] R. Daiyan, T. Tran-Phu, P. Kumar, K. Iputera, Z. Tong, J. Leverett, M. H. A. Khan, A. Asghar Esmailpour, A. Jalili, M. Lim, A. Tricoli, R. S. Liu, X. Lu, E. Lovell, R. Amal, *Energy Environ. Sci.* **2021**, *14*, 3588–3598.
[28] Y. Wang, W. Zhou, R. Jia, Y. Yu, B. Zhang, *Angew. Chem.* **2020**, *132*, 5388–5392.
[29] N. Meng, X. Ma, C. Wang, Y. Wang, R. Yang, J. Shao, Y. Huang, Y. Xu, B. Zhang, Y. Yu, *ACS Nano* **2022**, *16*, 9095–9104.
[30] G. F. Costa, M. Escudero-Escribano, *JACS Au* **2025**, *5*, 1538–1548.
[31] S. J. Ashton, *Design, Construction and Research Application of a Differential Electrochemical Mass Spectrometer (DEMS)*, Springer, Berlin, Heidelberg **2012**.
[32] A. C. Queiroz, M. L. Souza, M. R. Camilo, W. O. Silva, D. A. Cantane, I. Messias, M. R. Pinto, R. Nagao, F. H. B. Lima, *ChemElectroChem* **2022**, *9*, e202101408.
[33] J. Resasco, Y. Lum, E. Clark, J. Z. Zeledon, A. T. Bell, *ChemElectroChem* **2018**, *5*, 1064–1072.
[34] I. Messias, M. E. G. Winkler, G. F. Costa, T. Mariano, J. B. Souza Junior, I. T. Neckel, M. C. Figueiredo, N. Singh, R. Nagao, *ACS Appl. Energy Mater.* **2024**, *7*, 9034–9044.
[35] M. Rodrigues Pinto, R. E. Vos, R. Nagao, M. T. M. Koper, *J. Phys. Chem. C* **2024**, *128*, 21421–21429.
[36] F. Calle-Vallejo, *Curr. Opin. Electrochem.* **2023**, *42*, 101409.
[37] H. Muhammad Adeel Sharif, H. Muhammad Farooq Khan, S. Ullah, Y. Wang, M. Ahmad, B. Yang, C. Li, M. Bilal Asif, *J. Energy Chem.* **2024**, *95*, 380–406.
[38] Y. Yao, S. Zhu, H. Wang, H. Li, M. Shao, *Angew. Chem., Int. Ed.* **2020**, *59*, 10479–10483.
[39] G. E. Dima, A. C. A. de Vooys, M. T. M. Koper, *J. Electroanal. Chem.* **2003**, *554–555*, 15–23.
[40] M. Duca, M. C. Figueiredo, V. Climent, P. Rodriguez, J. M. Feliu, M. T. M. Koper, *J. Am. Chem. Soc.* **2011**, *133*, 10928–10939.
[41] I. Katsounaros, G. Kyriacou, *Electrochim. Acta* **2008**, *53*, 5477–5484.
[42] M. T. De Groot, M. T. M. Koper, *J. Electroanal. Chem.* **2004**, *562*, 81–94.
[43] H. Wang, D. R. Dekel, H. D. Abruña, *J. Am. Chem. Soc.* **2024**, *146*, 15926–15940.
[44] M. C. O. Monteiro, M. T. M. Koper, *Curr. Opin. Electrochem.* **2021**, *25*, 100649.
[45] H. Ooka, M. C. Figueiredo, M. T. M. Koper, *Langmuir* **2017**, *33*, 9307–9313.

Manuscript received: June 23, 2025
Revised manuscript received: August 19, 2025
Accepted manuscript online: August 30, 2025
Version of record online: ■■, ■■